JOURNAL OF GEOPHYSICAL RESEARCH, VOL. 109, A02305, doi:10.1029/2003JA010205, 2004

On the onset of HF-induced airglow at HAARP

E. V. Mishin
Boston College, Institute for Scientific Research, Chestnut Hill, Massachusetts, USA

W. J. Burke and T. Pedersen
Air Force Research Laboratory, Hanscom Air Force Base, Massachusetts, USA

Received 21 August 2003; revised 2 December 2003; accepted 19 December 2003; published 13 February 2004.

[1] Observations of airglow at 630 nm (red line) and 557.7 nm (green line) during the February 2002 campaign at the High Frequency Active Auroral Research Program (HAARP) heating facility are analyzed. We find that during injections toward magnetic zenith (MZ) the green and red lines gain ~5 R within ~1 s and ~20 R within ~10 s, respectively. We term this period the onset of the HF-induced airglow. A model of the onset at magnetic zenith is developed. It accounts for background photoelectrons and dissociative recombination of O_2^+. It is shown that heating and acceleration of background electrons dominate the airglow onset. We propose a scenario for the generation of strong Langmuir turbulence for injections outside the Spitze region, including magnetic zenith. *INDEX TERMS:* 2403 Ionosphere: Active experiments; 2483 Ionosphere: Wave/particle interactions; 2471 Ionosphere: Plasma waves and instabilities; 2481 Ionosphere: Topside ionosphere; *KEYWORDS:* HF modification experiments, artificial airglow onset

Citation: Mishin, E. V., W. J. Burke, and T. Pedersen (2004), On the onset of HF-induced airglow at HAARP, *J. Geophys. Res.*, *109*, A02305, doi:10.1029/2003JA010205.

1. Introduction

[2] A distinctive feature of HF modification experiments is the excitation of airglow at 630.0 and 557.7 nm by high-power, high-frequency (HF) radio waves [e.g., *Sipler et al.*, 1974; *Bernhardt et al.*, 1989; *Pedersen and Carlson*, 2001; *Gustavsson et al.*, 2001, 2002; *Kosch et al.*, 2000, 2002]. Enhancements up to ~500 R (Rayleighs) with the green-to-red ratio ζ_{gr} as high as $\geq$0.3 have been reported [*Gustavsson et al.*, 2002; *Kosch et al.*, 2002; *Pedersen et al.*, 2003]. The excitation energies ε_λ of the $O(^1D)$ and $O(^1S)$ states responsible for the red and green lines are ε_r = 1.96 eV and ε_g = 4.17 eV, respectively. The population of energetic, $\varepsilon > \varepsilon_\lambda$, electrons can increase significantly due to stochastic and resonant interactions with plasma turbulence generated by a heating wave [e.g., *Gurevich et al.*, 1985; *Dimant et al.*, 1992; *Mantas and Carlson*, 1996; *Gurevich and Milikh*, 1997; *Istomin and Leyser*, 2003]. The former raises the electron temperature T_e, the latter accelerates a group of electrons in the high-energy tail of the initial distribution. Both effects are well documented [e.g., *Carlson et al.*, 1982; *Gustavsson et al.*, 2001].

[3] *Gustavsson et al.* [2002] emphasized that to interpret $\zeta_{gr} > 0.1$ in terms of electron heating requires unrealizable $T_e > 2$ eV, pointing out the importance of electron acceleration. It is commonly believed that electrons are most efficiently accelerated by Langmuir (l) turbulence. The generation of Langmuir waves is usually described in terms of nonlinear instabilities of ordinary (o) mode pump waves, known as the parametric decay (PDI) or oscillating two-stream (OTSI) instabilities [*Fejer*, 1979]. In the presence of background suprathermal ($\varepsilon \gg T_e$) electrons, many more energetic electrons are accelerated than would be in Maxwellian plasmas [*Mishin and Telegin*, 1986].

[4] Recent observations show that the airglow maximizes during HF injections toward magnetic zenith [*Kosch et al.*, 2002; *Pedersen et al.*, 2003]. The same is true for the intensity of Langmuir waves [*Isham et al.*, 1999] and electron heating [*Rietveld et al.*, 2003] observed by the EISCAT UHF radar. Furthermore, the red line is excited at magnetic zenith even at extremely low effective radiative power $P_0 \sim 2$ MW [*Pedersen et al.*, 2003].

[5] Ordinary mode waves with incident angles θ outside the Spitze region, $\theta > \theta_c$, reflect at altitudes H_0 below the standard reflection altitude H_0 where the local plasma frequency $f_p \simeq 10^4\sqrt{n_e}$ Hz equals the driver frequency f_0. Here $\theta_c = \arcsin(\sqrt{\frac{f_c}{f_c+f_0}}\sin\chi)$, f_c is the local electron gyrofrequency, n_e is the electron density in cm^{-3}, and χ is the magnetic dip angle [e.g., *Mjølhus*, 1990]. At HAARP $\chi \simeq 14.5°$ and $f_c \simeq 1.4$ MHz at altitudes near 200 km, so that for f_0 = 7 MHz the Spitze angle is $\theta_c \simeq 5.9°$.

[6] Figure 1 shows a schematic of ray trajectories for ordinary HF waves injected vertically and toward magnetic zenith into a horizontally stratified ionosphere at HAARP. Obliquely incident radiation does not form standing-wave patterns and swelling is absent. Thus, given P_0 = 150 MW and distance R = 250 km, the wave amplitude is $E_0 \simeq 4.7\sqrt{P_0}/R \simeq 0.2$ V/m. With f_0 = 7 MHz and T_e = 0.1 eV, the HF energy density at the reflection point is $W_0 = \frac{E_0^2}{4\pi} \simeq 10^{-4} n_e T_e$, sufficient to drive the PDI/OTSI at H_0 [*Fejer*,

0148-0227/04/2003JA010205$09.00

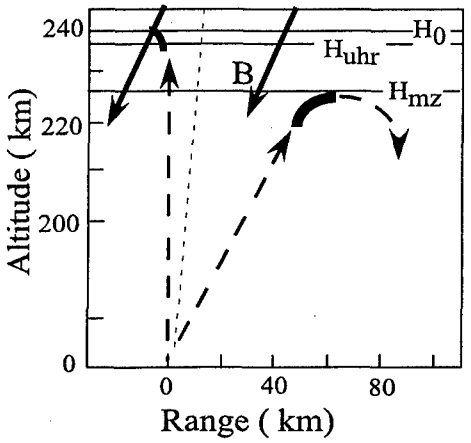

Figure 1. Schematic of ray propagation for ordinary HF waves injected toward local vertical and magnetic zenith. The magnetic field **B** direction is indicated by arrows. The heights of reflection and upper hybrid resonance are shown by horizontal lines. A light dashed line shows the Spitze angle direction. The regions of excitation of Langmuir turbulence appear as bold lines near the reflection points.

1979]. However, mismatch of frequencies at $H_0 < H_0$ suppress these instabilities for injections outside the Spitze region.

[7] *Gurevich et al.* [2002] suggested that decreased plasma densities within striations generated by heating waves permit necessary phase matching [cf. *Muldrew*, 1978]. Changes in the refraction index (self-focusing) due to striations develop within tens of seconds after turn-on and explain some features of the spatial distribution of the HF-induced airglow. However, the rise time of Langmuir waves is ~10 ms [*Isham et al.*, 1999]. Besides, striations are generated in the upper hybrid layer [e.g., *Vaskov et al.*, 1981; *Lee and Kuo*, 1983]. Hence the reflection height of the heating wave must be at or above this height. For magnetic-zenith injections at HAARP, this can be satisfied only if $f_0 \leq 5.4$ MHz. However, the strongest airglow at HAARP occurred with higher f_0 values [*Pedersen et al.*, 2003].

[8] *Kuo et al.* [1997] showed that Langmuir waves can be excited by upper hybrid (*uh*) waves with amplitudes exceeding the threshold value $E^{l}_{uh} \sim 0.15$ V/m. Such *uh*-waves can be generated through the linear conversion of the *o*-mode on pre-existing field-aligned irregularities [*Wong et al.*, 1981] or through the parametric decay $o \rightarrow uh + lh$ [e.g., *Istomin and Leyser*, 1995]; *lh* stands for lower hybrid waves. Linear conversion within the upper hybrid layer proceeds with no set threshold. However, the parametric decay develops if $E_0 > E_0^{uh} \simeq 1.6\, \tilde{f}_0^2$ mV/m, provided that the inequality $0.015 < |f_0 - s \cdot f_c| < 0.5$ MHz (integer $s \geq 3$) is valid. Here $\tilde{f}_0$ stands for the heating frequency in MHz. The rise time of the *uh*-wave is $\tau_{uh} \sim 1-3$ ms. Consistent with observations [*Isham et al.*, 1999], this makes the generation of Langmuir turbulence possible within ~10 ms.

[9] Besides electron impact, dissociative recombination (DR) of O_2^+ is an efficient source of the $O(^1D)$ and $O(^1S)$ states. Since the rate of dissociative recombination decreases with T_e, it is usually not considered in the theory of the HF-induced airglow. However, the quantum yield for the $O(^1S)$ state from dissociative recombination grows significantly with T_e and with the vibrational temperature of oxygen ions [*Guberman*, 1997; *Peverall et al.*, 2001]. Furthermore, charge exchange $O^+ + O_2 \rightarrow O_2^+ + O$ is the dominant source of O_2^+ production in the nighttime *F* region. Its rate increases significantly whenever O_2 is vibrationally excited [*Viggiano and Williams*, 2001]. We expect a high degree of excitation of molecular species in the HF-illuminated region and thus enhanced yields of the green line emissions.

[10] A consistent theory of the HF-induced airglow accounting for the ion/neutral chemistry, modification of the heated spot, and self-focusing has yet to be worked out. We emphasize that responsible processes develop within tens of seconds. However, considerable airglow appears within first few seconds after the HF transmitter turns on. We designate this interval as the onset of HF-induced airglow.

[11] This paper develops a model for the onset of airglow enhancements at magnetic zenith accounting for the roles of O_2^+ dissociative recombination and energetic photoelectrons. The following section describes the onset characteristics from the HF heating experiments at HAARP. Section 3 describes the model. In particular, we propose a scenario (section 3.3) for the generation of strong Langmuir turbulence outside the Spitze region including magnetic zenith with upper hybrid waves as the primary source. The final section compares modeling results with optical measurements.

2. Airglow Onset: HAARP, February 2002

[12] The HAARP facility is located outside of Gakona Alaska (62.4°N, 145.15°W). During the course of HF heating experiments between 03:00 and 05:00 UT in February 2002 several passes of Defense Meteorological Satellite Program (DMSP) satellites flew to the east and west of the HAARP location. Each of these spacecraft carries a pair of upward looking particle spectrometers designed to measure fluxes of downcoming electrons and ions with energies between 30 eV and 30 keV. Consistent with prevailing quiet geomagnetic ($Kp = 2$) conditions, the equatorward boundary of auroral precipitation was several degrees in latitude poleward of Gakona. However, both before and after the local time of sunset, the spectrometers detected fluxes of Rdowncoming electrons whose spectra monotonically decreased with energies between 30 and 100 eV. These subauroral fluxes consist of photoelectrons that originated in the still sunlit southern ionosphere.

[13] Intense green-line emissions were observed between 03:48 and 05:00 UT (17:48–19:00 LT) on February 13, 2002 events of the HAARP optics campaign. Readers are referred to the report of *Pedersen et al.* [2003] for graphic examples of HAARP- induced airglow and the intensities of red/green-line emissions recorded during the period of interest. *O*-mode waves were injected toward magnetic zenith at $f_0 = 7.8$ MHz and at full power of 0.94 MW ($P_0 \simeq 165$ MW). The transmitter was programmed to turn on for 5 minutes exactly on the minute. Subsequent pulses followed 5 minutes pauses. However, the fourth pulse in the sequence started at 04:21:18 UT. A transmitter problem produced a false start, 04:30:00–04:31:00 UT, prior to the long pulse that began at 04:32:12 UT. In the course of this long pulse, the critical frequency of the *F* layer dropped

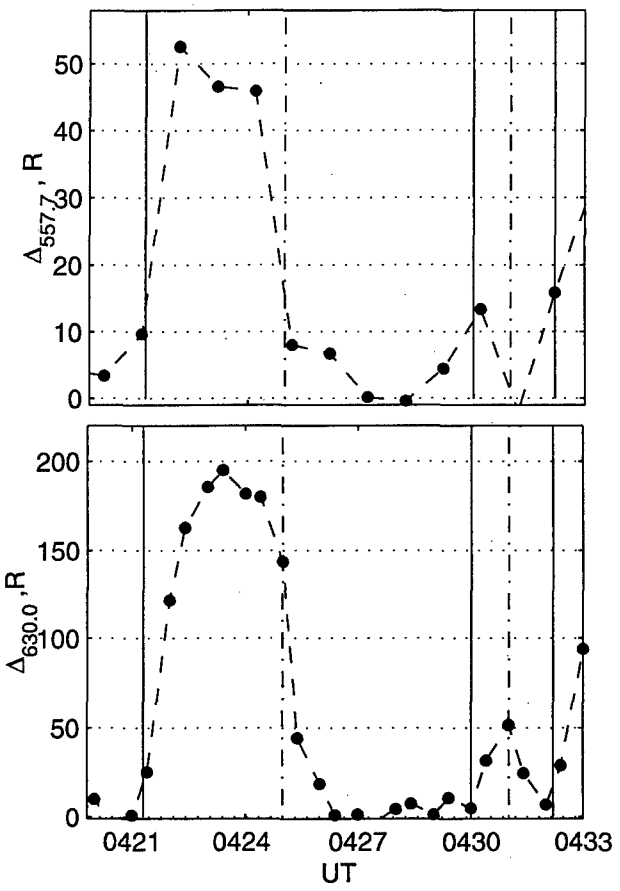

Figure 2. Heater-induced green (top panel) and red (bottom panel) lines during February 13, 2002 injections. Vertical solid and dash-dotted lines indicate heater turn-ons and turn-offs, respectively.

below the transmitter frequency and the sequence was terminated.

[14] To account for natural (background) variations, a polynomial fit was made to intensities measured along the magnetic meridian in each all-sky image, with the heated area blocked out. Throughout the studied period the difference between the background airglow b_λ and that of the heated volume I_λ, during heater-off periods, was less than ~3–5 and ~7–10 R for green- and red-line emissions, respectively. This small difference determines the accuracy of heater-induced airglow measurements $\Delta_\lambda = I_\lambda - b_\lambda$.

[15] Figure 2 presents a detailed view of the last three HF-induced enhancements of February 13, 2002 at f_0 = 7.8 MHz. Data points are from two red line exposures compiled at 0 and 24 s after the beginning of each minute, and green-line exposure beginning at 12 s into the minute. After 04:00 UT, the exposure duration was 7.5 s. By examining cases when the heater turned on part way through an exposure, we see that the green-line emissions increased by ~5 (~10) R within ~1.5 (~7.5) s, while the red line gained ~25 (~30) R within ~13.5 (~20.5) s.

[16] Starting at 04:27:15 UT on February 9, 2002, a $P_0 \simeq$ 124 MW wave at a frequency 6.8 MHz was injected toward magnetic zenith. Figure 3 shows red- and green-line emissions before and during the pulse turn on from the heated volume and the background region. These data show that the difference between natural green-line emissions from magnetic zenith and ~70 km apart was less than 1 R. The same is true for the red-line emission before the heater turned on. This suggests that the background airglow was nearly uniform. When the heater turned on, green (red)-line intensities increased by ~5 (~30) R within ~4.5 (~16.5) s. It is relevant to note that *Kosch et al.* [2002] reported ~500 R enhancements of the red- and green-line emissions produced by the EISCAT superheater (P_0 ~ 600 MW) within the first 5-s frame.

3. Modeling Airglow Onset

[17] For modeling purposes we assume that the major species constituents of the neutral atmosphere and ionospheric plasma are well described by the MSIS-E [*Hedin*, 1991] and IRI [*Bilitza*, 2001] models, respectively. Although photodissociation of O_2 accounts for ~50% of the background airglow, it is unaffected by heating and hence is not included. Basic processes and their rate coefficients are discussed at length by *Solomon et al.* [1988], *Rees* [1989], *Witasse et al.* [1999], and *Fox and Sung* [2001]. Unless

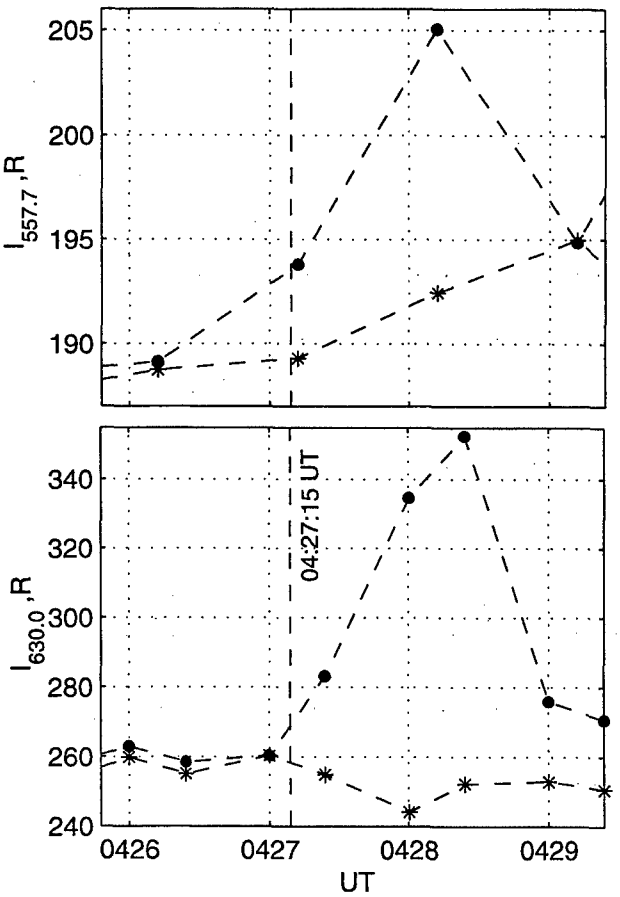

Figure 3. Heater-induced green (top) and red (bottom) lines during February 9, 2002 injections. Dots and asterisks stand for emissions from the magnetic zenith and background regions, respectively. Vertical dashed line indicates the heater turn-on time.

otherwise noted, we use the rate coefficients of *Fox and Sung* [2001].

[18] As mentioned above, radiative emissions from a heated volume reflect the superposed results of complex wave, plasma, and chemical interactions. To render our modeling of this complex chain of interactions intelligible, we divide this section into three parts. The first subsection concerns the basic contributors to the natural and artificially excited radiation budgets. The subsection on the background ionosphere estimates the distributions of ion species and energetic photoelectrons present at heater altitudes prior to turn on. The third subsection describes a flow chart encapsulating our concept of how heater-injected energy is transformed into the various wave modes that heat and/or accelerate ambient electrons that interact with ambient neutrals to produce onset green- and red-line emissions.

3.1. Basic Processes

[19] The red (r) and green (g) line-photons are emitted by atomic oxygen in the transition from the $O(^1D)$ and $O(^1S)$ states to $O(^3P)$ and $O(^1D)$ states, respectively. In photochemical equilibrium, the volume emission rate η_λ is calculated from

$$\eta_\lambda^{eq} = A_\lambda \cdot [O_\lambda] = A_\lambda \frac{Q_\lambda}{L_\lambda + A_{\Sigma\lambda}} \quad (1)$$

Here $[O_\lambda]$ stands for the density of $O(^1D)$ or $O(^1S)$ in cm^{-3}; Q_λ and L_λ are the corresponding production and loss rates, respectively; $A_r \simeq 0.007$, $A_{\Sigma r} \simeq 0.009$, $A_g \simeq 1.2$, and $A_{\Sigma g} \simeq 1.3$ are the Einstein transition probabilities in s^{-1}. The column emission rate (in R) is found by integrating (1) along the line of sight

$$4\pi I_\lambda = 10^{-6} \int_{z_0}^{z_1} \eta_\lambda(z)\, dz \quad (2)$$

[20] The rates of electron impact excitation $O + e \rightarrow O(^1D, ^1S) + e$ and the Schumann-Runge dissociation $O_2 + e \rightarrow O + O(^1D) + e$ are calculated as follows

$$Q_\lambda^e = [O] \cdot \varkappa_\lambda^e = [O] \cdot 4\pi \int_{\varepsilon_\lambda}^{\infty} \sigma_\lambda(\varepsilon)\Phi(\varepsilon) d\varepsilon \quad (3)$$

Here $\Phi(\varepsilon)$ is the electron differential number flux, $\varkappa_\lambda^e$, ε_λ, and σ_λ are the rate coefficients, threshold energies, and cross-sections, respectively. We employ electron impact cross-sections suggested by *Majeed and Strickland* [1997]. Figure 4 shows three of the major electron impact cross sections. It is worth noting that $\varkappa_r^e(T_e)$ and $\varkappa_g^e(T_e)$ calculated with a Maxwellian distribution of thermal electrons are close to the approximations used by *Mantas and Carlson* [1996] and *Gurevich and Milikh* [1997], respectively.

[21] The dissociative recombination of O_2^+ produces $Q_\lambda^{DR} = \varkappa_\lambda^{DR} n_e [O_2^+]$. The rate coefficients are usually approximated as $\varkappa_\lambda^{DR} = \beta_\lambda^{DR} \cdot \alpha$, where β_λ^{DR} are the quantum yields. Estimated yields for $O(^1S)$ were subject to substantial discrepancy in the literature for many years. Recent experiments [*Kella et al.*, 1997; *Peverall et al.*, 2001; A. Petrignani et al., Vibrationally resolved rate coefficients and branching in the dissociative recombination of O_2^+, submitted to *Journal of Chemical Physics*, 2003] and theory

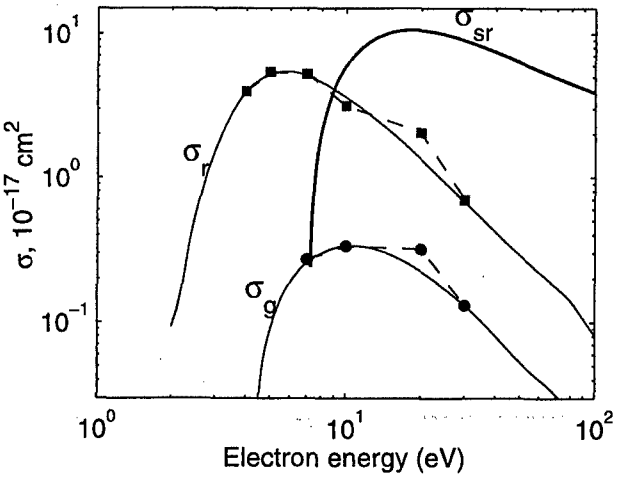

Figure 4. Cross-sections of the $O(^1D)$ and $O(^1S)$ excitation and the Schumann-Runge dissociation by direct electron impact. Squares and dots are the measured cross-sections from *Doering and Gulcicek* [1989]; solid lines are interpolations by *Majeed and Strickland* [1997].

[*Guberman*, 1988, 1997] appear to have reconciled this controversy. They established that α and β_λ^{DR} depend not only on T_e but also on the vibrational population $n_{O_2^+}^{(j)} = [O_2^+(j)]/[O_2^+]$ of O_2^+, where $j = 0, 1, \ldots$ designates the vibrational level.

[22] For the ground vibrational state, $\beta_r^{(0)} \simeq 1.15$, $\alpha^{(0)} \simeq 2\ 10^{-7}\tau_e^{-0.63}$ [cf. *Fox and Sung*, 2001], and

$$\beta_g^{(0)} \simeq 0.063 \exp\left(-\frac{2.23}{\tau_e}\left(1 - \frac{0.39}{\tau_e}\right)\right) \quad (4)$$

for $1 \leq \tau_e \leq 10$, where $\tau_e = T_e[K]/300$. Importantly, the inequalities $\beta_g^{(1,2)} > \beta_g^{(0)}$ and $\beta_r^{(1,2)} < \beta_r^{(0)}$ hold. For the Maxwell-Boltzmann distribution of $N_{O_2^+}^{(j)}$ with vibrational temperatures $T_V \sim 0.25$ eV, one obtains $\beta_g^{DR} \sim 1.2\beta_g^{(0)}$ and $\beta_r^{DR} \sim 0.85\beta_r^{(0)}$.

[23] Collisional quenching $O^\# + X \rightarrow O + X$ is important for the $O(^1D)$ state, while for $O(^1S)$ at altitudes >150 km it can be ignored. Here X stands for O, O_2, N_2, or e_{th}. The corresponding loss rates are $L_r^X = 10^{-11}\ \varkappa_X^q [X]$, where $\varkappa_O^q \simeq 0.65\ \tau_n^{0.14}$, $\varkappa_{O_2}^q \simeq 3.2 \exp(0.225/\tau_n)$, $\varkappa_{N_2}^q \simeq 1.8 \exp(0.36/\tau_n)$, and $\varkappa_e^q \simeq 28.7\ \tau_e^{0.91}$. Figure 5 shows the altitude profile of the total loss rate calculated with the MSIS-E and IRI parameters at 04:30 UT, February 13, 2002.

[24] Finally, the radiative cascade (RC) $O(^1S) \rightarrow O(^1D) + h\nu_{5577}$ yields $Q_r^{RC} = \eta_g$.

3.2. Background Ionosphere

[25] Simultaneous observations from a digisonde located at the HAARP site were used to correct the IRI model and to determine that the reflection height at magnetic zenith decreased from ~250 to ~235 km between 04:00 and 04:30 UT on February 13, 2002. At the same time, the shadow height increased from ~150 to ~230 km indicating the presence of photoelectrons [e.g., *Doering et al.*, 1975]. Furthermore, the southern-hemisphere region magnetically conjugate to HAARP remained in sunlight, even after local sunset. Thus a large fraction of the photoelectron spectrum

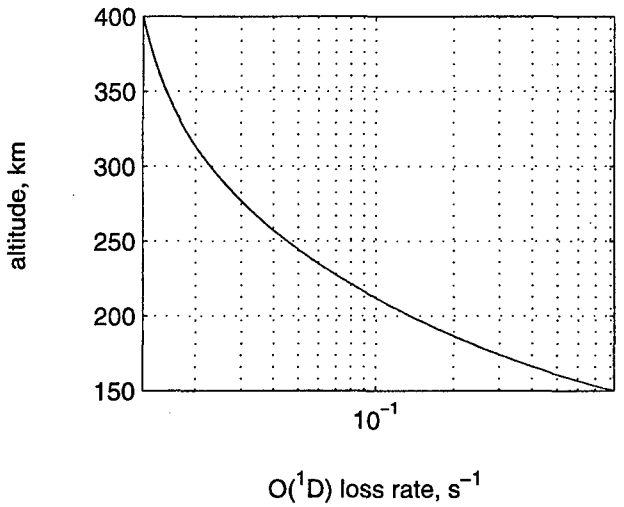

Figure 5. $O(^1D)$ loss rate.

generated in the conjugate ionosphere [e.g., *Peterson et al.*, 1977] had access to the ionosphere above HAARP. Electron spectrometers on DMSP satellites observed the high-energy tail of the conjugate photoelectron spectrum.

[26] Figure 6 shows altitude profiles of the background electron temperature T_0 and electron and O^+ densities calculated from the corrected IRI model. The twilight O_2^+ density above ~200 km is defined by the charge exchange and dissociative recombination

$$[O_2^+] \simeq \varkappa_{ce} \frac{[O_2]\,[O^+]}{\alpha\, n_e} \tag{5}$$

Here the rate of charge exchange $\varkappa_{ce}$ after *Viggiano and Williams* [2001] is

$$\begin{aligned} \varkappa_{ce} &\simeq \varkappa_{ce}^{(0)}\left(n_{O_2}^{(0)} + n_{O_2}^{(1)}[4.9\lg(\tau_{in}+1) - 2.5]\right) \\ \varkappa_{ce}^{(0)} &\simeq 10^{-11}\left(\frac{2.2}{\tau_{in}^{0.52}} + 6.05\exp\left(-\frac{34.04}{\tau_{in}}\right)\right), \end{aligned} \tag{6}$$

α is the recombination rate in cm^3/s, $n_{O_2}^{(j)} = [O_2(j)]/[O_2]$, $[Y]$ stands for the density of species Y in cm^{-3}, and $\tau_{in} = 1.5\tau_i + \tau_n - 1$ with $\tau_{i,n} = T_{i,n}[\mathrm{K}]/300$.

[27] The IRI model predicts $T_e = T_0 \leq 0.2$ eV (Figure 6). At these temperatures and $n_e > 10^5$ cm^{-3}, a Maxwellian distribution F_M is a good representation of the thermal electron distribution function (F_{th}) in the F region [*Mishin et al.*, 2000]. The differential number flux $\Phi_s(\varepsilon)$ of photoelectrons in the F region [e.g., *Rees*, 1989] at $\varepsilon \geq \varepsilon_s = \frac{1}{2}mv_s^2 \sim 5$ eV can be approximated by a power-law function

$$\Phi_s(\varepsilon) = \frac{p_s - 0.5}{4\pi\varepsilon_s} n_s v_s \left(\frac{\varepsilon_s}{\varepsilon}\right)^{p_s} \tag{7}$$

where $n_s \leq 100$ cm^{-3} and $p_s \simeq 3$.

3.3. HF-Perturbed Ionosphere

[28] Our scenario for the excitation of plasma turbulence and subsequent electron energization in the HF-illuminated region at magnetic zenith is represented schematically in Figure 7. First, upper hybrid waves are generated due to the parametric decay $o \rightarrow uh + lh$. Its threshold field is $E_0^{uh} \sim 0.08$ V/m if the matching conditions are met at $x_{uh} = k_{uh}^2 r_e^2 < 1$, where r_e is the thermal electron gyroradius and k_{uh} is the uh-wave vector. Landau damping of short-scale lower hybrid waves raises the threshold otherwise [*Mishin et al.*, 1997]. For $f_0 = 7.8$ (6.8) MHz and $\theta \simeq 14.5°$, the matching conditions at the reflection height H_0 are easily satisfied for $x_{uh} \simeq 0.3$ ($\simeq$0.15). Finally, the free space field of the incident wave $E_0 \simeq 0.25$ (0.2) V/m exceeds E_0^{uh}.

[29] When the amplitude of the primary uh-wave E_{uh} exceeds ~10 mV/m, it excites other, lower frequency, uh-wave with the growth rate of order $\gamma_{uh} \sim \tau_{uh}^{-1}$ [*Zhou et al.*, 1994]. The same is true for subsequently generated uh-waves. The frequency-step of this spectral transfer is quite small $|\delta\omega_{uh}|/\omega_{uh} \sim 0.1 x_{uh}\delta k_{uh}/k_{uh} \sim 0.2\sqrt{m_e/m_i}$, where m_e/m_i represents the electron/ion mass ratio. As many spectral steps occur before the parametric instability saturates, the resulting uh-energy spectrum consists of a large number $\Lambda \gtrsim 10$ of spectral peaks, each of order $E_0^2/(\gamma_{uh}\tau_{uh})$ (well-known weak turbulence "cascading" [e.g., *Sagdeev et al.*, 1991]). Thus the total uh-energy density can be estimated as $W_*/\Lambda \sim W_0 \simeq 7.5$ (5) eV/cm^3 with the r.m.s amplitude $E_* \simeq \sqrt{4\pi W_*} \sim \sqrt{\Lambda}E_0$.

[30] Upper hybrid waves with amplitudes E_{uh} exceeding the threshold value $E_{uh}^l \simeq 0.1/x_{uh}^{1/2}$ V/m generate short-scale, $k_l > 3^{-1/2}/r_e$, Langmuir waves [*Kuo et al.*, 1997]. Due to a weak dependence of the growth rate γ_l on k_{uh}, one can take $E_{uh} \sim E_*$. As this value greatly exceeds the threshold E_{uh}^l, the growth rate can be evaluated as $\gamma_l \sim \nu_e E_{uh}/E_{uh}^l$ [*Kuo et al.*, 1997], which amounts to $\gamma_l \sim \nu_e\sqrt{10^2 x_{uh}\Lambda E_0^2}$. Here ν_e is the electron elastic (transport) collision frequency.

[31] The growth of Langmuir waves at $T_e/T_i \leq 4$ saturates via induced scattering by ions that transfers energy toward

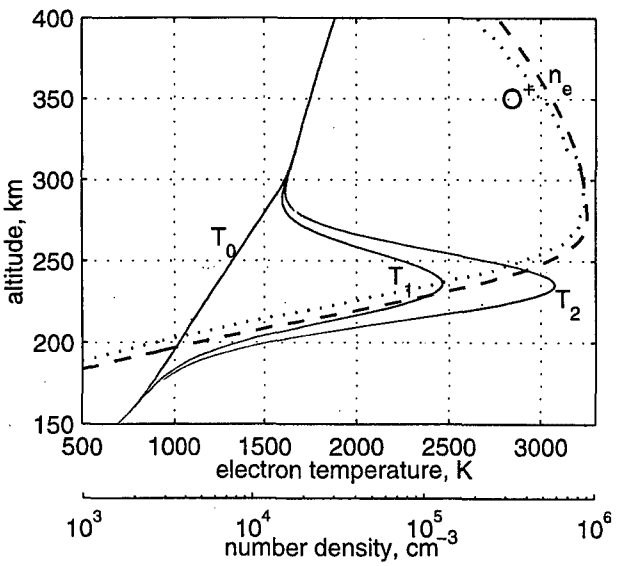

Figure 6. Altitude profiles of the electron temperature (solid lines), electron density (dashed line), and O^+ density (dotted line). T_0, T_1, and T_2 stand for 0, 1, and $\simeq$1.5 s after turn-on.

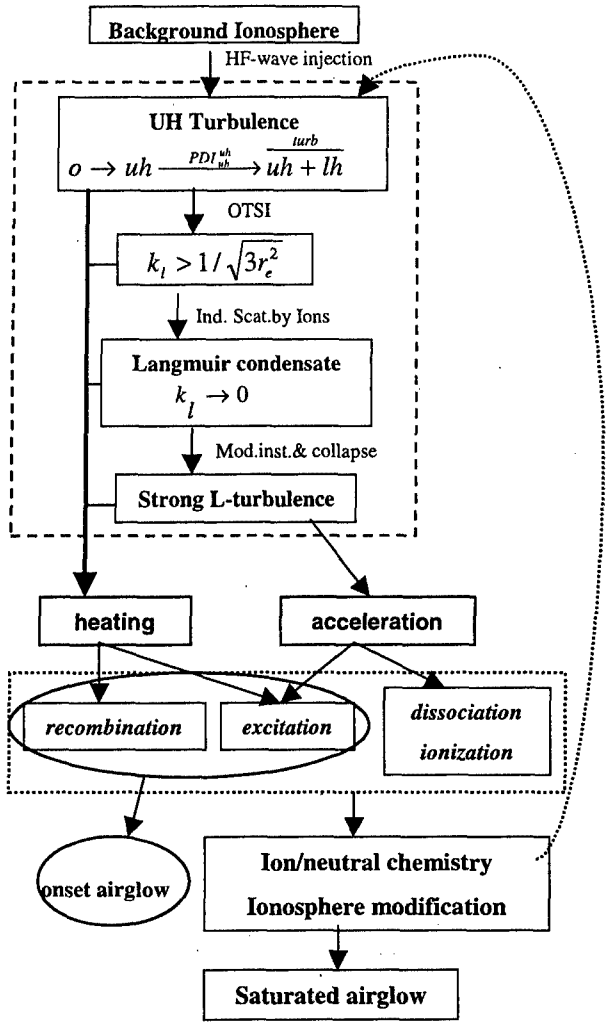

Figure 7. Block-diagram showing synergy of a model of HF-induced airglow at magnetic zenith. Shaded boxes indicate the steps to be worked out.

small k [e.g., *Zakharov et al.*, 1976]. This process is governed by the pump *uh*-wave power. In particular, if the width Δk_l of the parametrically unstable *l*-wave spectrum exceeds $\Delta k_c \simeq k_l \nu_e/\gamma_l$, the Langmuir wave energy W_l accrues in a state with $k \rightarrow 0$ (Langmuir condensate) [*Zakharov et al.*, 1976; *Zakharov*, 1984]. The spectral width can be evaluated as $\Delta k_l \sim 3(f_0/f_c)^2 W_*/(n_e T_e r_e)$. Thus, for $E_0 > 0.15(\tilde{f}_0 \nu_e)^{1/6}/\sqrt{\Lambda} \lesssim 0.2$ V/m the "condensate" condition $\Delta k_l > k_l \nu_e/\gamma_l$ is fulfilled. The dynamics of the Langmuir condensate is defined by the modulational instability and collapse leading to establishment of strong (cavitating) Langmuir turbulence [e.g., *Galeev et al.*, 1977; *Zakharov*, 1972, 1984].

[32] We emphasize that this applies not only at the reflection layer H_0 but also well below it, wherever the matching conditions for the parametric decay $o \rightarrow uh + lh$ are met and local values of $x_{uh} < 1$. Given the plasma density profile shown in Figure 6 and $f_0 \sim 6$–8 MHz, the altitude extent of this region is ~10 km. One should compare this value with a few 100-m size of the Airy pattern at H_0, where the PDI/OTSI instabilities develop during injections within the Spitze region [*Fejer*, 1979]. We believe that this is the key factor in exciting strong airglow at magnetic zenith.

3.3.1. Heating

[33] Collisional damping of high-frequency *o*-, *uh*-, and *l*-waves is the major source of (stochastic) electron heating. *Mishin et al.* [2000] showed that at $[N_2] > 10^7 \tilde{f}_0^2$ cm^{-3} the process of N_2-vibrational excitation dominates the formation of the distribution function of ionospheric electrons with energies $3.5 \geq \varepsilon > \varepsilon_{vib} \simeq 1.8$ eV, which can be represented as follows

$$F_{th}(\varepsilon > \varepsilon_{vib}) \simeq F_M\left(\frac{\varepsilon + \varepsilon_{vib}}{2}\right)\sqrt{\frac{\varepsilon^{0.5}\kappa(\varepsilon_{vib})}{\varepsilon_{vib}^{0.5}\kappa(\varepsilon)}} \times \exp\left[-\frac{1}{\sqrt{2T_e}}\int_{\varepsilon_{vib}}^{\varepsilon} \xi^{-1/2}\kappa(\xi)d\xi\right] \quad (8)$$

Here $\kappa^2(\varepsilon) = \nu_{il}(\varepsilon)/\nu_{ee}(\varepsilon) + 0.5\varepsilon/T_e$, where ν_{il}/ν_{ee} is the ratio between electron inelastic and electron-electron collision frequencies. A total HF wave energy density $W_{HF} \ll 10^{-2} n_0 T_e$ is assumed. At energies $\varepsilon < \varepsilon_{vib}$ the distribution is close to F_M, while at $\varepsilon > 3.5$ eV it may slightly deviate from F_M due to the $O(^1D)$ and $O(^1S)$ excitation.

[34] The electron temperature can be evaluated from the energy balance

$$1.5 n_e \partial T_e/\partial t = \Gamma_e - \nu_e \delta \cdot n_e T_e - \nabla_{\parallel} q_{e\parallel} \quad (9)$$

where $q_{e\parallel}$ is the (parallel) electron heat flux, $\Gamma_e \simeq \nu_e W_{HF}$ is the volume heating rate, and $\delta = \langle \nu_{il}/\nu_e \rangle$ is the coefficient of inelastic losses averaged over the total distribution F_{th}.

[35] Given $\nu_e \sim 500$ s^{-1}, Γ_e is $\gtrsim$40 (25) keV/cm^3/s. Note that to match their optical observations, *Mantas and Carlson* [1996] used the values of Γ_e between $\simeq$50 and $\simeq$125 keV/cm^3/s at ~260 km for $f_0 \simeq 5$ MHz. *Gustavsson et al.* [2001] used $\Gamma_e \simeq 60$ keV/cm^3/s for $f_0 \simeq 4$ MHz to fit the electron temperature profile maximum 4000 K at ~220 km observed by the EISCAT UHF radar. Neither of them accounted for the decrease of $\delta(T_e)$ due to the deviation of the thermal electron distribution from Maxwellian. Taking that into account, the calculation results of *Mantas and Carlson* [1996] and *Gustavsson et al.* [2001] can be scaled to the $T_{1,2}$-profiles in Figure 6, pertaining to our case.

3.3.2. Acceleration

[36] Resonant *lh*- and *l*-wave-particle interaction accelerates electrons. *Musher et al.* [1978, 1986] analyzed in detail the dynamics of *lh*-waves excited by an external source. At $1 < T_e/T_i \leq 4$, high-frequency waves, $f_{lh} > f_c\sqrt{2m_e/m_i}$, are dominated by induced scattering by ions. The rate of spectral transfer toward smaller frequencies is $\tilde{\gamma}_{lh} \sim (f_c^2/f_{lh})W_{lh}/n_0 T_e$, where W_{lh} is the energy density of lower hybrid waves. Equating the growth rate γ_{uh} to $\tilde{\gamma}_{lh}$ yields the energy density at the saturated state $W_{lh}^0/n_0 T_e \sim \gamma_{uh} f_{lh}/f_c^2 \sim 10^{-5.5}$.

[37] The dynamics of *lh*-waves in the low-frequency, $f_{lh} < f_c\sqrt{2m_e/m_i}$, region is dominated by the lower hybrid collapse [e.g., *Musher et al.*, 1978]. The threshold energy density is quite low $W_{lh}^c/nT_e \simeq x_{lh}(m_e/m_i)(f_c/f_0)^2 \leq 10^{-6}$, and is surely exceeded in our case. In the course of collapse, the longitudinal and transverse dimensions of a *lh*-cavity,

$l_\parallel \sim l_\perp \sqrt{m_i/x_{lh} m_e}$, diminish. Finally, the *lh*-wave energy in a collapsing cavity is absorbed by particles via Landau damping [*Musher et al.*, 1978, 1986; *Sotnikov et al.*, 1978; *Shapiro et al.*, 1993]. The density of accelerated electrons in the magnetic field-aligned high-energy tail of the distribution function, determined by assuming resonant particles carry away all of the energy pumped into collapsing cavities [e.g., *Shapiro et al.*, 1993], is of order $<10^{-5} n_e$. This *lh*-contribution appears insufficient to account for the observed HF-induced airglow. It is worth noting that *lh*-collapse also leads to transversely accelerated ions that absorb the collapsing energy at approximately the same rate as electrons [*Sotnikov et al.*, 1978].

[38] Strong Langmuir turbulence consists of an ensemble of collapsing cavitons that transfer the wave energy toward small scales. Small-scale, $k \geq \omega_k/v_{\min}$, waves are absorbed by fast $v \geq v_{\min} \gg \sqrt{T_e/m_e}$ electrons via Landau damping, thereby increasing the population of suprathermal electrons. The distribution of accelerated electrons $F_a(\varepsilon) = \frac{m^2}{2\varepsilon}\Phi_a(\varepsilon)$ in weakly magnetized $f_c \ll f_p$ plasmas can be found from the kinetic equation [e.g., *Galeev et al.*, 1977]

$$\frac{\partial F_a}{\partial t} = \frac{1}{v^2}\frac{\partial}{\partial v}\left[\frac{\omega_k^4}{mnv}\int_{\omega_k/v}^{\infty}\frac{W_k}{k^3}dk\frac{\partial F_a}{\partial v}\right] \tag{10}$$

where $\omega_k/(2\pi) \sim f_p$ and W_k are, respectively, the frequency and spectral energy density of Langmuir waves. The latter is determined from the requirement for energy balance

$$\frac{dW_k}{dt} + \frac{d}{dk}\left[W_k\frac{dk}{dt}\right] = \Gamma_k W_k \tag{11}$$

Here

$$\Gamma_k = -\left(\frac{2\pi^2}{n_0}\right)\left(\frac{\omega_k^4}{k^3}\right)F_a\left(\frac{\omega_k}{k}\right) \tag{12}$$

is the rate of Landau damping; $k(t) \sim (t_c - t)^{-2}$ is defined by the collapse law in the absorption region [*Pelleiter*, 1982], and t_c is the collapse time.

[39] The steady state solution of (10)–(12) at $\varepsilon \geq \varepsilon_{\min} = \frac{1}{2}m_e v_{\min}^2$ is a power-law function [*Pelleiter*, 1982; *Shapiro and Shevchenko*, 1984] that yields the differential number flux

$$\Phi_a(\varepsilon) = \frac{p_a - 0.5}{4\pi\varepsilon_{\min}} n_a v_{\min}\left(\frac{\varepsilon_{\min}}{\varepsilon}\right)^{p_a} \tag{13}$$

($p_a \simeq 0.75$). One-dimensional (magnetically field-aligned) numerical modeling of electron acceleration by strong Langmuir turbulence yields $\Phi_a(\varepsilon_\parallel) \sim \varepsilon_\parallel^{-1}$, consistent with the 1D scaling law for Langmuir collapse [*Galeev et al.*, 1983; *Wang et al.*, 1997]. A flat distribution of accelerated electrons is consistent with the observations of *Carlson et al.* [1982].

[40] The minimum energy $\varepsilon_{\min}$ and the density of particles in the high-energy tail n_a are determined by the boundary condition

$$\Phi_a(\varepsilon_{\min}) = \Phi_0(\varepsilon_{\min}) \tag{14}$$

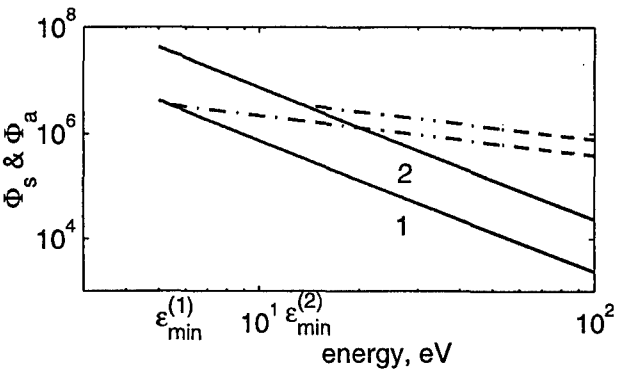

Figure 8. Differential number fluxes of photoelectrons (solid lines) and accelerated electrons (dash-dotted lines) in $cm^{-2}s^{-1}ster^{-1}eV^{-1}$ for $n_s = 1$ (line 1) and 10 (line 2) cm^{-3}.

and the wave energy flux transferred by collapsing cavitons and absorbed by accelerated particles

$$\omega_p\left(\frac{m_e}{m_i}\frac{|E_{k_m}^2|}{24\pi n_0 T_e}\right) \simeq -\Gamma_{k_m} \tag{15}$$

Here E_{k_m} is the wave amplitude in a cavity of the scale length $l_{\min} \sim k_m^{-1} \simeq v_{\min}/\omega_p$ when collapse is arrested and Φ_0 is the differential number flux of ionospheric electrons.

[41] For a Maxwellian electron distribution, one has $\varepsilon_{\min}^M \sim 20T_e$. When photoelectrons are present, $\Phi_0(\varepsilon) \rightarrow \Phi_s(\varepsilon)$ at $\varepsilon \gg T_e$, and $\varepsilon_{\min}$ is defined by

$$\varepsilon_{\min}^s \sim 30(n_s T_e/W_l)^{2/5}\ \text{eV} \tag{16}$$

valid for the energy density of Langmuir turbulence $W_l \gg n_0 T_e m_e/m_i$ [*Mishin and Telegin*, 1986]. Given $n_s = 10\ cm^{-3}$, $n_e = 6\ 10^5\ cm^{-3}$, and $W_l \simeq 10^{-4} n_e T_e$, from (16) one gets $\varepsilon_{\min}^s \simeq 15$ eV. The number of accelerated electrons exceeds the photoelectron background in the energy range $\varepsilon > \varepsilon_{\min}^s$ by a factor of $\frac{p_s - 0.5}{p_a - 0.5} \sim 10$. For energies $\varepsilon \leq \varepsilon_{\min}^s$, the distribution is unaffected. Figure 8 shows differential number fluxes of photoelectrons (7) and accelerated electrons (13) for $n_s = 1$ and 10 cm^{-3}, $n_e = 6\ 10^5\ cm^{-3}$, and $W_l \simeq 10^{-4} n_e T_e$.

4. Discussion

[42] Figure 9 shows the components of the equilibrium volume emission rates $\eta_\lambda^{eq}(1)$ for the period near 0430 UT. To calculate the contributions of photoelectrons (7) and accelerated electrons (13), $n_s = 10\ cm^{-3}$ and $W_l \simeq 10^{-4} n_e T_2$ were chosen, yielding $\varepsilon_{\min}^s \simeq 15$ eV for $f_0 = 7.8$ MHz. As expected from (4), the dissociative recombination contribution to the red line is reduced much more than that for the green line. Apparently, heated electrons dominate the red-line emission, while accelerated electrons are the major contributor to the green line. Note a factor of about 2 difference between calculations with $F_M(T_1)$ and $F_{th}(T_1)$ consistent with *Mishin et al.* [2000] (it is $\simeq$3.5 for $T_e = T_2$).

[43] In the heated volume the densities of excited oxygen atoms and of O_2^+ ions grow. During the onset period $[O(^1D)]$ and $[O_2^+]$ remain well below the new equilibrium values that

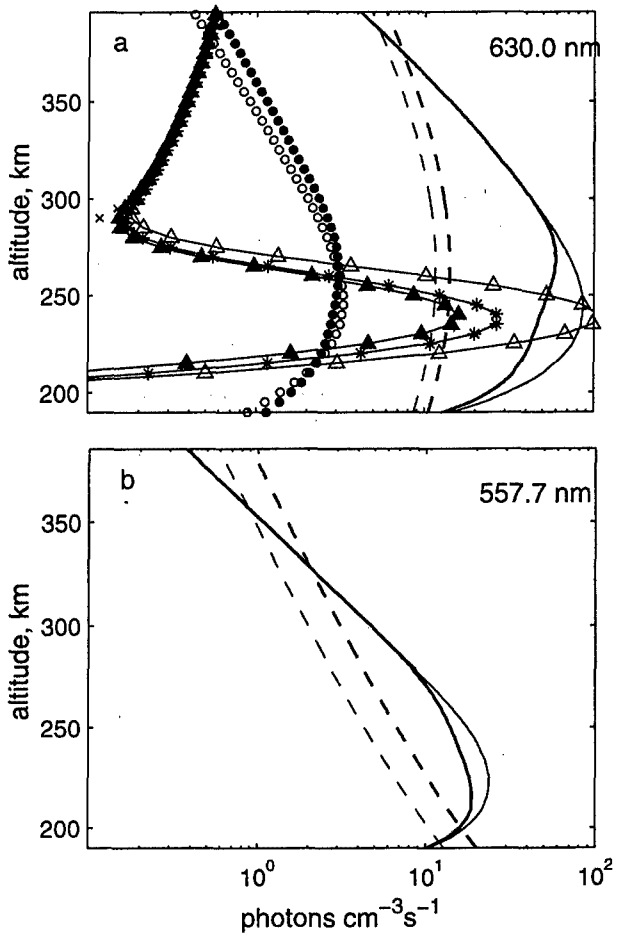

Figure 9. Equilibrium volume emission rate components of the red (a) and green (b) emissions: Dissociative recombination with $[O_2^+]_0$ from the background $T_e = T_0$ (thin solid line) and heated $T_e = T_2$ (bold solid line) regions; photoelectrons (thin dashed line) and accelerated electrons (bold dashed line); $O(^1S)$ cascading from the background (circles) and heated (dots) regions; thermal electrons with $T_e = T_0$ (crosses), T_1 (filled triangles), and T_2 (open triangles); Maxwellian electrons with $T_e = T_1$ (asterisks).

are of the order of Q_r/L_r and $\varkappa_{ce}$ $[O_2]/\alpha(T_2)$, respectively. Corresponding time-variations of the contributing components to the total volume emission rate during the onset can be evaluated assuming that $A_{\Sigma g} < \zeta < \min[1/(n_e\alpha_2), 1/L_r] \simeq$ 15 s and $L_r \simeq \text{const}(t)$ at 200–300 km. Here $\zeta = t - t_0$ and the heating time $t_0 \sim 1$ s. As a result, one gets

$$\delta[O_2^+] = [O_2^+]/[O_2^+]_0 - 1 \simeq n_e[\alpha(T_0) - \alpha(T_2)] \cdot \zeta \qquad (17)$$

This yields

$$\eta_g(\zeta) \simeq \eta_g^{eq} + \eta_g^{DR} n_e[\alpha(T_0) - \alpha(T_2)] \cdot \zeta$$
$$\eta_r(\zeta) \simeq (\eta_r^{eq} L_r + 0.5\eta_r^{DR}[L_r + n_e\alpha(T_2)]\delta[O_2^+])\zeta \qquad (18)$$

[44] Using (18) and Figure 9, the variation of the red- and green-line emissions during the onset period are calculated from (2). The results are shown in Figure 10 together with the observed intensities (section 2). There is good apparent agreement with the HAARP observations.

[45] We emphasize that the onset values of the HF-induced airglow amount to $\lesssim$10% of the saturated values. As the reflection heights of 7.8 and 6.8 MHz waves at magnetic zenith are below the upper hybrid resonance, similar to Figure 1, striations are not generated. Thus self-focusing due to striations seems unlikely. This indicates that the ionosphere's parameters in the heated volume are significantly modified. Apparently, a complete explanation of artificially induced airglow involves a complex chain of plasma and chemical interactions within the heated volume and has yet to be worked out.

5. Conclusion

[46] Observations of airglow at 630 nm (red line) and 557.7 nm (green line) acquired during the February 2002 campaign at the HAARP heating facility have been analyzed. During injections toward magnetic zenith the intensities of green and red line emissions gain ~5–10 R within ~1 s and ~20 R within ~10 s, respectively. We call this period the onset of HF-induced airglow and develop an explanatory model for the growth of emissions from magnetic zenith. The model accounts for the roles played by ambient photoelectrons and dissociative recombination of O^+ ions and shows that heating and acceleration of background electrons, possibly by strong Langmuir turbulence, dominate the airglow onset.

[47] We also propose a new scenario for the generation of strong Langmuir turbulence for injections outside the Spitze region, including magnetic zenith, with upper hybrid waves as the primary source of Langmuir waves. Those waves accumulate in the region of small wavevectors due to induced scattering by ions (Langmuir condensate). Waves in the condensate are subject to the modulational instability and collapse thus leading to strong turbulence. This scenario

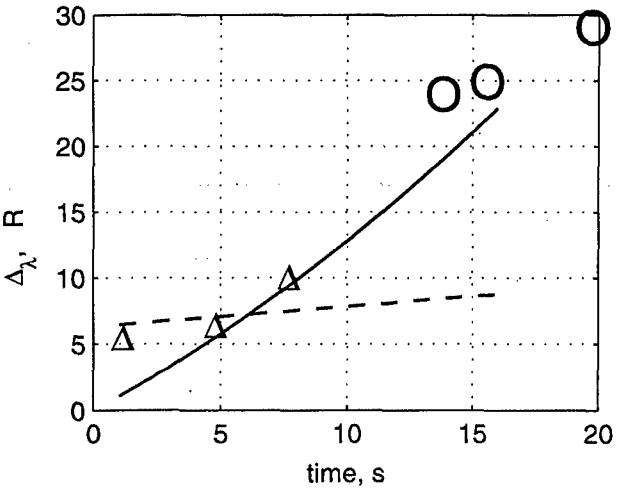

Figure 10. Calculated intensities of the HF-induced red (solid line) and green (dashed line) emissions during the onset period. The observed intensities are shown by open circles (red) and triangles (green), respectively.

applies not only at the reflection layer but also well below it, wherever the matching conditions for the parametric decay $o \rightarrow uh + lh$ are met and local values of $x_{uh} < 1$. For injections toward magnetic zenith and heating frequencies $\geq$5.4 MHz, this occurs below the altitude of the upper hybrid resonance. The large altitude extent of the strong turbulence region appears to be the key factor in exciting strong airglow at magnetic zenith.

[48] **Acknowledgments.** This research was supported in part by the HF Active Auroral Research Program (HAARP) under AFRL contract F19628-02-C-0012 with Boston College and by Air Force Office of Scientific Research under tasks 2311AS and 2311SD.

[49] Arthur Richmond thanks Bjorn Gustavsson and Michael T. Rietveld for their assistance in evaluating this paper.

References

Bernhardt, P., C. Tepley, and L. Duncan (1989), Airglow enhancements associated with plasma cavities formed during ionospheric heating experiments, *J. Geophys. Res.*, *94*, 9071.

Bilitza, D. (2001), International Reference Ionosphere 2000, *Radio Sci.*, *36*, 261.

Carlson, H., V. Wickwar, and G. Mantas (1982), Observations of fluxes of suprathermal electrons accelerated by HF excited Langmuir instabilities, *J. Atmos. Terr. Phys.*, *12*, 1089.

Dimant, Y., A. Gurevich, and K. Zybin (1992), Acceleration of electrons under the action of intense radio-waves near electron cyclotron harmonics, *J. Atmos. Terr. Phys.*, *54*, 425.

Doering, J., and E. Gulcicek (1989), Absolute differential and integral electron excitation cross sections for atomic oxygen: The $^3P \rightarrow {}^1D$ and $^3P \rightarrow {}^1S$ transitions from 4.0 to 30 eV, *J. Geophys. Res.*, *94*, 1541.

Doering, J., W. Peterson, C. Bostrom, and J. Armstrong (1975), Measurement of low-energy electrons in the day airglow and day side auroral zone from Atmosphere Explorer C, *J. Geophys. Res.*, *80*, 3934.

Fejer, J. (1979), Ionospheric modification and parametric instabilities, *Rev. Geophys.*, *17*, 135.

Fox, J., and K. Sung (2001), Solar activity variations of the Venus thermosphere/ionosphere, *J. Geophys. Res.*, *106*, 21,305.

Galeev, A., R. Sagdeev, V. Shapiro, and V. Shevchenko (1977), Langmuir turbulence and dissipation of high-frequency energy, *Sov. Phys. JETP*, *46*, 711.

Galeev, A., R. Sagdeev, V. Shapiro, and V. Shevehenko (1983), Beam plasma discharge and suprathermal electron tails, in *Active Experiments in Space (Alpbach, Austria)*, Eur. Space Agency Spec. Publ., ESA-SP-195, p. 151.

Guberman, S. (1988), The production of $O(^1D)$ from dissociative recombination of O_2^+, *Planet. Space Sci.*, *36*, 47.

Guberman, S. (1997), Mechanism for the green glow of the upper atmosphere, *Science*, *278*, 1276.

Gurevich, A., and G. Milikh (1997), Artificial airglow due to modifications of the ionosphere by powerful radio waves, *J. Geophys. Res.*, *102*, 1389.

Gurevich, A., Y. Dimant, G. Milikh, and V. Vaskov (1985), Multiple acceleration of electrons in the regions high-power radio-wave reflection in the ionosphere, *J. Atmos. Terr. Phys.*, *47*, 1057.

Gurevich, A., K. Zybin, H. Carlson, and T. Pedersen (2002), Magnetic zenith effect in ionospheric modifications, *Phys. Lett. A*, *305*(5), 264.

Gustavsson, B., et al. (2001), First tomographic estimate of volume distribution of HF-pump enhanced airglow emission, *J. Geophys. Res.*, *106*, 29,105.

Gustavsson, B., B. Brändström, A. Steen, T. Sergienko, T. Leyser, M. Rietveld, T. Aso, and M. Erjii (2002), Nearly simultaneous images of HF-pump enhanced airglow at 6300 Å and 5577 Å, *Geophys. Res. Lett.*, *29*(24), 2220, doi:10.1029/2002GL015350.

Hedin, A. (1991), Extension of the MSIS thermospheric model into the middle and lower atmosphere, *J. Geophys. Res.*, *96*, 1159.

Isham, B., M. Rietveld, T. Hagfors, C. LaHoz, E. Mishin, W. Kofman, T. Leyser, and A. van Eyken (1999), Aspect angle dependence of HF enhanced incoherent backscatter, *Adv. Space Res.*, *24*(8), 1003.

Istomin, Y., and T. Leyser (1995), Parametric decay of an electromagnetic wave near electron cyclotron harmonics, *Phys. Plasmas*, *2*, 2084.

Istomin, Y., and T. Leyser (2003), Electron acceleration by cylindrical upper hybrid oscillations trapped in density irregularities in the ionosphere, *Phys. Plasmas*, *10*, 2962.

Kella, D., L. Vejby-Christenson, P. Jonson, H. Pedersen, and L. Andersen (1997), The source of green line emission determined from a heavy-ion storage ring experiment, *Science*, *276*, 1530.

Kosch, M., M. Rietveld, T. Hagfors, and T. Leyser (2000), High-latitude HF-induced airglow displaced equatorward of the pump beam, *Geophys. Res. Lett.*, *27*, 2817.

Kosch, M., B. Gustavsson, and M. Rietveld (2002), An overview of high-latitude induced aurora from EISCAT, paper presented at World Space Congress, Am. Inst. of Aeron. and Astron., Houston, Tex.

Kuo, S., M. Lee, and P. Kossey (1997), Excitation of oscillating two stream instability by upper hybrid pump in ionospheric heating experiments at Tromsø, *Geophys. Res. Lett.*, *24*, 2969.

Lee, M., and S. Kuo (1983), Excitation of upper hybrid waves by a thermal parametric instability, *J. Plasma Phys.*, *30*, 30,463.

Majeed, T., and D. J. Strickland (1997), New survey of electron impact cross sections for photoelectron and auroral electron energy loss calculations, *J. Phys. Chem. Ref. Data*, *26*, 335.

Mantas, G., and H. Carlson (1996), Reinterpretation of the 6300-Å airglow enhancements observed in the ionosphere heating experiments based on analysis of Plateville, Colorado, data, *J. Geophys. Res.*, *101*, 195.

Mishin, E., and V. Telegin (1986), Spectrum of suprathermal electrons in the auroral plasma, *Sov. J. Plasma Phys.*, *12*, 509.

Mishin, E., T. Hagfors, and W. Kofman (1997), On origin of outshifted plasma lines during HF modification experiments, *J. Geophys. Res.*, *102*, 27,265.

Mishin, E., H. Carlson, and T. Hagfors (2000), On the electron distribution function in the F region and airglow enhancements during HF modification experiments, *Geophys. Res. Lett.*, *27*, 2857.

Mjølhus, E. (1990), On linear conversion in a magnetized plasma, *Radio Sci.*, *25*, 1321.

Muldrew, D. (1978), The role of field-aligned ionization irregularities in the generation of the HF-induced plasma line at Arecibo, *J. Geophys. Res.*, *83*, 2552.

Musher, S., A. Rubenchik, and B. Sturman (1978), Collective effects associated with lower hybrid heating of plasma, *Plasma Phys.*, *20*, 1131.

Musher, S., A. Rubenchik, and I. Shapiro (1986), Nonlinear effects in the propagation of an ion beam across a magnetic field, *Sov. Phys. JETP*, *63*, 519.

Pedersen, T., and H. Carlson (2001), First observations of HF heater-produced airglow at the High Frequency Active Auroral Research Program facility: Thermal excitation and spatial structuring, *Radio Sci.*, *36*, 1013.

Pedersen, T., M. McCarrick, E. Gerken, C. Selcher, D. Sentman, H. Carlson, and A. Gurevich (2003), Magnetic zenith enhancement of HF radio-induced airglow production at HAARP, *Geophys. Res. Lett.*, *30*(4), 1169, doi:10.1029/2002GL016096.

Pelleiter, G. (1982), Generation of a high-energy electron tail by strong Langmuir turbulence in a plasma, *Phys. Rev. Lett.*, *49*, 782.

Peterson, W., J. Doering, T. Potemra, R. McEntire and C. Bostrom (1977), Conjugate photoelectron fluxes observed on Atmosphere Explorer C, *Geophys. Res. Lett.*, *4*, 109.

Peverall, R., et al. (2001), Dissociative recombination and excitation of O_2^+: Cross sections, product yields and implications for studies of ionospheric airglows, *J. Chem. Phys.*, *114*, 6679.

Rees, M. (1989), *Physics and Chemistry of the Upper Atmosphere*, Cambridge Univ. Press, New York.

Rietveld, M., M. Kosch, N. Blagoveshchenskaya, V. Kornienko, T. Leyser, and T. Yeoman (2003), Ionospheric electron heating, optical emissions and striations induced by powerful HF radio waves at high latitudes: Aspect angle dependence, *J. Geophys. Res.*, *108*(A4), 1141, doi:10.1029/2002JA009543.

Sagdeev, R., V. Shapiro, and V. Shevchenko (1991), Anomalous dissipation of strong electromagnetic waves in a laser plasma, in *Physics of Laser Plasma*, vol. 3, edited by A. Rubenchik and S. Witkowski, p. 271, North-Holland, New York.

Shapiro, V., and V. Shevchenko (1984), Strong turbulence of plasma oscillations, in *Basic Plasma Physics*, edited by A. Galeev and R. Sudan, vol. 2, p. 123, North-Holland, New York.

Shapiro, V., V. Shevchenko, A. Sharma, K. Papadopoulos, R. Sagdeev, and V. Lebedev (1993), Lower-hybrid turbulence at cometary bow wave and acceleration of cometary protons, *J. Geophys. Res.*, *98*, 1325.

Sipler, D., E. Enemark, and M. Biondi (1974), 6300-Å intensity variations produced by the Arecibo ionospheric modification experiment, *J. Geophys. Res.*, *79*, 4276.

Solomon, S., P. Hays, and V. Abreu (1988), The auroral 6300 Å emission: Observation and modeling, *J. Geophys. Res.*, *93*, 9867.

Sotnikov, V., V. Shapiro, and V. Shevchenko (1978), Macroscopic effects of collapse at lower hybrid resonanse, *Sov. J. Plasma Phys.*, *4*, 250.

Vaskov, V. V., A. Gurevich, and A. N. Karashtin (1981), Thermal self-focusing instability of plasma waves near resonance, *Geomagn. Aeron., Engl. Transl.*, *21*, 724.

Viggiano, A., and S. Williams (2001), Ion-molecule kinetics at high temperatures (300–1800 K): Derivation of internal energy dependencies, *Adv. Gas-Phase Ion Chem.*, *4*, 85.

Wang, J., D. Newman, and M. Goldman (1997), Vlasov simulations of electron heating by Langmuir turbulence near the critical altitude in the radiation-modified ionosphere, *J. Atmos. Sol. Terr. Phys.*, *59*, 2461.

Witasse, O., J. Lilensten, and C. Lathuillére (1999), Modeling of the OI 630.0 and 557.7 nm thermospheric dayglow during EISCAT-WINDII coordinated measurements, *J. Geophys. Res.*, *104*, 24,639.

Wong, A., G. J. Morales, D. Eggleston, J. Santoru, and R. Behnke (1981), Rapid conversion of electromagnetic waves to electrostatic waves in the ionosphere, *Phys. Rev. Lett.*, *47*, 1340.

Zakharov, V. (1972), Collapse of Langmuir waves, *Sov. Phys. JETP*, *35*, 908.

Zakharov, V. (1984), Collapse and self-focusing of Langmuir waves, in *Basic Plasma Physics*, edited by A. Galeev and R. Sudan, vol. 2, p. 81, North-Holland, New York.

Zakharov, V., S. Musher, and A. Rubenchik (1976), Weak Langmuir turbulence of an isothermal plasma, *Sov. Phys. JETP*, *42*, 80.

Zhou, H., J. Huang, and S. Kuo (1994), Cascading of the upper hybrid/electron Bernstein wave in ionospheric heating experiments, *Phys. Plasmas*, *1*, 3044.

W. J. Burke and T. Pedersen, Air Force Research Laboratory, Space Vehicles Directorate, Hanscom Air Force Base, MA 01731, USA. (william.burke@hanscom.af.mil; todd.pedersen@hanscom.af.mil)

E. V. Mishin, Boston College, Institute for Scientific Research, 402 St. Clements Hall, 140 Commonwealth Avenue, Chestnut Hill, MA 02467-3862, USA. (evgenii.mishin@hanscom.af.mil)

REPORT DOCUMENTATION PAGE

Form Approved
OMB No. 0704-0188

1. REPORT DATE *(DD-MM-YYYY)*
13-06-2005

REPRINT

4. TITLE AND SUBTITLE
On the Onset of HF-induced Airglow at HAARP

5a. CONTRACT NUMBER

5b. GRANT NUMBER

5c. PROGRAM ELEMENT NUMBER
61102F

6. AUTHOR(S)
E.V. Mishin*, W.J. Burke and T. Pedersen

5d. PROJECT NUMBER
2311

5e. TASK NUMBER
SD

5f. WORK UNIT NUMBER
A3

7. PERFORMING ORGANIZATION NAME(S) AND ADDRESS(ES)
Air Force Research Laboratory/VSBXP
29 Randolph Road
Hanscom AFB MA 01731-3010

8. PERFORMING ORGANIZATION REPORT NUMBER
AFRL-VS-HA-TR-2005-1061

9. SPONSORING / MONITORING AGENCY NAME(S) AND ADDRESS(ES)

10. SPONSOR/MONITOR'S ACRONYM(S)

11. SPONSOR/MONITOR'S REPORT NUMBER(S)

12. DISTRIBUTION / AVAILABILITY STATEMENT
Approved for Public Release; Distribution Unlimited.

*Boston College, Institute for Scientific Research, Chestnut Hill, MA

13. SUPPLEMENTARY NOTES
REPRINTED FROM: JOURNAL OF GEOPHYSICAL RESEARCH, Vol 109, A02305,
doi: 10.1029/2003JA010295, 2004.

14. ABSTRACT

[1] Observations of airglow at 630 nm (red line) and 557.7 nm (green line) during the February 2002 campaign at the High Frequency Active Auroral Research Program (HAARP) heating facility are analyzed. We find that during injections toward magnetic zenith (MZ) the green and red lines gain ~5 R within ~1 s and ~20 R within ~10 s, respectively. We term this period the onset of the HF-induced airglow. A model of the onset at magnetic zenith is developed. It accounts for background photoelectrons and dissociative recombination of O_2^+. It is shown that heating and acceleration of background electrons dominate the airglow onset. We propose a scenario for the generation of strong Langmuir turbulence for injections outside the Spitze region, including magnetic zenith.

15. SUBJECT TERMS
Wave/particle interactions
HF modification experiments
Topside ionosphere
Artificial airglow onset

16. SECURITY CLASSIFICATION OF:			17. LIMITATION OF ABSTRACT	18. NUMBER OF PAGES	19a. NAME OF RESPONSIBLE PERSON
a. REPORT		c. THIS PAGE			W. Burke
UNCLAS	UNCLAS	UNCLAS	SAR		19b. TELEPHONE NUMBER *(include area code)* 781-377-3980